Available online at www.sciencedirect.com
ScienceDirect
Journal of Power Sources 165 (2007) 232–243
JOURNAL OF POWER SOURCES
www.elsevier.com/locate/jpowsour

Non-isothermal transient modeling of water transport in PEM fuel cells

Hao Wu [a], Peter Berg [b,*], Xianguo Li [a]

[a] *Department of Mechanical Engineering, University of Waterloo, Waterloo, Ont., Canada*
[b] *Faculty of Science, University of Ontario Institute of Technology, Oshawa, Ont., Canada*

Received 17 October 2006; received in revised form 29 November 2006; accepted 30 November 2006
Available online 12 January 2007

Abstract

Dynamic responses of PEM fuel cells are crucial for mobile applications such as in automobiles. There are four main transient processes in a PEM fuel cell, namely, species transport, electric double layer charge/discharge, membrane hydration/dehydration, and heat transfer. In this study, a rigorous transient model has been developed, accounting for all four transient mechanisms. The dynamic characteristics have been analyzed, corresponding to various changes in working conditions, such as relative humidity and/or cell voltage. Moreover, by using three different membrane types, Nafion 112, Nafion 115, and Nafion 117, the effect of membrane thickness on the cell dynamic performance has been investigated, and the importance of heat transfer effects on the cell dynamic responses have been highlighted.

Keywords: Transient; PEMFCs; Water transport; Heat transfer

1. Introduction

With the increasing concerns of sustainable energy and environmental issues, polymer electrolyte membrane fuel cells (PEMFCs) are attracting more attention from the public and governments. The implementation of PEMFCs, replacing traditional combustion engines in automobiles, promises a potential clean-energy future. In the past decade, significant improvements have been achieved and trial buses, driven by PEMFCs, are in successful operation around the world. However, many technical barriers still remain to be resolved before fuel cell power systems can be extensively commercialized. For example, the freeze startup of PEMFCs at subzero temperature conditions is a complex problem for automobile applications. It entails three-phase modeling (in the gas diffusion layer), namely ice, liquid water and water vapour. Only a complete study involving all three phases is able to predict timescales of freeze startups as well as the negative impacts on reliability and durability of subzero operation. In this study, only a single phase is considered, providing the building blocks for future multi-phase flow modeling.

In our previous work [1], a two-dimensional isothermal model is developed to investigate the transient phenomena in a fully humidified PEMFC. In the fully humidified case, the membrane hydration process is of no concern, and the cell dynamic performance is determined by the transport of the reactant gas species and the electrical double layer charge/discharge process only. Our analysis indicates that the time scale for the electrical double layer charge/discharge process is on the order of 10 μs; the time scale of species transport is longer, but still within 2 s, even at severely flooded conditions. Therefore, the cell presents excellent dynamic characteristics in the fully humidified case. However, experimental observation in our laboratory suggests that the dynamic response time in an actual operating cell is much longer, and is of the order of minutes, perhaps due to the combined effect of slow membrane water uptake, liquid water formation in the GDL, and heat transfer processes. Hence, a more comprehensive transient model is required to account for the water transport and heat transfer processes.

The water transport in PEM fuel cells entails two competing effects: on one side, the membrane electrical conductivity increases with the membrane water content; thus the membrane should be as hydrated as possible to facilitate the proton transport. On the other side, however, excess water may accumulate in the cathode gas pore and catalyst layer, and block the oxygen transport, which causes a significant concentration overpotential loss. A dynamic water balance is hence necessary for a sound operation of the cell. In general, two modeling approaches of membrane water transport exist: hydraulic models and diffusive

* Corresponding author. Tel.: +1 905 721 3111; fax: +1 905 721 3304.
E-mail address: peter.berg@uoit.ca (P. Berg).

0378-7753/$ – see front matter © 2006 Elsevier B.V. All rights reserved.
doi:10.1016/j.jpowsour.2006.11.061

Nomenclature

a	water activity; density of active area in the catalyst layer ($m^2\ m^{-3}$)
c	molar concentration ($mol\ m^{-3}$)
c_p	specific heat ($J\ kg^{-1}\ K$)
d_h	hydraulic diameter (m)
D	mass diffusivity of species ($m^2\ s^{-1}$)
F	Faraday's constant 96487 ($C\ mol^{-1}$)
h_m	mass transfer coefficient ($m\ s^{-1}$)
h_T	heat transfer coefficient ($W\ m^{-2}\ K$)
$j_{0,ref}$	reference exchange current density ($A\ m^{-3}$)
$\vec{J}$	phase current density ($A\ m^{-2}$)
k	thermal conductivity ($W\ m^{-1}\ K$)
n	number of electrons transferred in the half cell reaction; unit normal vector
n_d	electro-osmotic drag coefficient (H_2O/H^+)
Nu	Nusselt number
P	pressure (atm)
Q	heat source ($J\ m^{-3}$)
$\Re$	universal gas constant 8.314 ($J\ mol^{-1}\ K$)
R_i	reaction rate ($A\ m^{-3}$)
RH	relative humidity
S	source terms, entropy ($J\ K^{-1}$)
Sh	Sherwood's number
t	time (s)
T	temperature (K)

Greek letters

α	transfer coefficient
ε	porosity
η	overpotential (V)
λ	membrane water content
ρ	density ($kg\ m^{-3}$)
σ	electrical conductivity ($S\ m^{-1}$)
$\mathcal{W}$	equivalent molecular weight of dry membrane ($1.1\ kg\ mol^{-1}$)
$\Im$	relative humidity

Subscripts and superscripts

a	anode
act	activation
c	cathode
eff	effective value
g	gas phase
i	the ith species
m	membrane; mass transfer
k	source term of species
ohm	ohmic
ref	reference state
rev	reversible
s	solid phase; species transport
sat	saturation pressure (atm)
T	source term of temperature
w	water vapor
wm	membrane water
ϕ	source term of charge
0	standard conditions (273 K and 1 atm); inlet conditions

models. In the hydraulic model, the convective flow of liquid water caused by a pressure gradient is included. However, experimental work [2] has shown that the application of a pressure difference between the cathode and anode did not have a large effect upon the drag coefficient, which is contrary to what is suggested by the hydraulic model. Hence, the diffusive model is more frequently employed in the literature. Springer et al. [3] were one of the pioneers working with the diffusive membrane hydration mechanisms. They implemented a one-dimensional isothermal model which accounts for the variation of membrane water content. Empirical correlations between the water activity and membrane water content are developed based on experimental data measured at 30 °C. Other transport properties such as the water diffusivity and membrane electrical conductivity are considered as functions of membrane water content. Independently, Yang [4] developed an empirical expression that related the membrane water content with water activity based on their experimental results, which correspond to the results of Springer et al. Kulikovsky [5] used a new set of correlations based on the experimental work of Hinatsu et al. [6] which were measured at 80 °C, and implemented a model similar to Springer et al., which differentiates the water transport in the membrane from the water vapor transport in the GDL and gas channel. In the catalyst layer (CL), two phases are coupled together through an equilibrium assumption and the PEM water concentration is converted to the water vapor concentration through mathematical relations. Using a similar mathematical technique, Um and Wang [7] proposed a single-domain water transport model which converts the water concentration in the electrolyte to water vapor concentration both in the catalyst layer and the membrane layer, and the resulting water transport equation can be casted into a general form which is valid for the whole domain. This approach is also employed in the present study and a more detailed description of this approach will be given in the next section. It should be noted that all of the above mentioned models assume that the hydronium (or proton) concentration in the membrane is constant, and only the water concentration varies spatially in the membrane. Berg et al. [8] established a model which accounted for the hydronium concentration variation in the membrane. Several fitted parameters are explored to simplify their model. Most recently, Baschuk and Li [9] derived a more general membrane model. They considered the membrane as being composed of a mixture of solid matrix, hydronium ions and liquid water, and described the transport phenomena in the membrane using the Stephen–Maxwell equation.

A heat transfer sub-model is also necessary for a rigorous transient analysis. Compared to water transport, heat transfer in the cell is much easier to model and, hence, there is less discrepancy in the literature. However, almost all physical parameters and transport processes are related to temperature. To reduce the

computational complexities of the system, heat transfer effects are neglected by most of the researchers. Ju et al. [10] presented a single phase non-isothermal model which coupled the heat transfer with electrochemical reactions and mass transport. A parametric study on the GDL thermal conductivity is conducted and the heat release in each part of the cell is analyzed in detail. The authors conclude that the thermal effects become more critical at higher current density and/or lower GDL thermal conductivity. In the work of Rowe and Li [11], the heat transfer in the cell is considered as the combination of the following two mechanisms: conductive heat transfer in the solid matrix; and convective heat transfer in the pores, with local thermodynamic equilibrium between the two phases. The heat generation/adsorption effects during the water phase change are also taken into account in this work. Berning et al. [12] later presented a similar conductive-convective heat transfer model. In their model, the temperature in solid and fluid phases are solved independently, and a relatively arbitrary heat transfer coefficient is used to account for the heat exchange between the two phases.

Most of the above-mentioned studies treated the water and thermal management separately and none of them dealt with the transient phenomena of PEMFCs. Reviewing the literature, we found that most of the studies are focused on steady state modeling and very few of them concentrated on transient phenomena. Berg et al. [13] presented a transient discharge model for the cathode, and used it for parameter tuning and determination of liquid water in the membrane electrode assembly (MEA). Stumper et al. [14] used a similar approach to determine the MEA resistance and electrode diffusion coefficient. Natarajan and Nguyen [15] presented a two-dimensional two-phase transient model for the cathode. Both multi-species flow and capillary flow of liquid water are accounted for in their model. Wang and Wang [16] developed a three-dimensional, single-phase model for the whole cell; the evolution of water accumulation and the corresponding dynamic responses of the cell performance are studied. However, all above-mentioned transient models are isothermal and none of them investigated the cell as a water transport and thermally coupled system.

Therefore, the objective of the present study is to develop a comprehensive transient model which incorporates water transport and heat transfer in the cell, and to investigate the effect of dynamically changing operating condition, such as a dynamic change in cell potential or relative humidity, on the cell performance.

2. Model formulation

In this study, a two-dimensional modeling domain, identical to our previous study [1], is adopted and shown in Fig. 1. The convective flow in the gas flow channel is not considered in the present model since the flow direction is normal to the 2D modeling plane. The detailed description of mass and charge transfer processes were illustrated in [1]. Therefore, only those matters related to water transport and heat transfer will be elucidated in this study.

2.1. Water transport

In the present study, a pseudo two-phase water transport model similar to Springer and Kulikovsky's approach is used. That is, adsorbed water is present in the electrolyte and vapor in the GDL. In the catalyst layer, both phases coexist in local thermodynamical equilibrium. The mechanisms of water transport are schematically shown in Fig. 1(a).

In the GDL, the phase change of water is neglected and water exists as vapor only. Furthermore, due to the two-dimensional nature of the current model (cross-plane model), convection between the gas channel and the catalyst layer is also ignored, with the convection at the interface between gas flow channel and GDL taken care of via mass transfer coefficients in the bound-

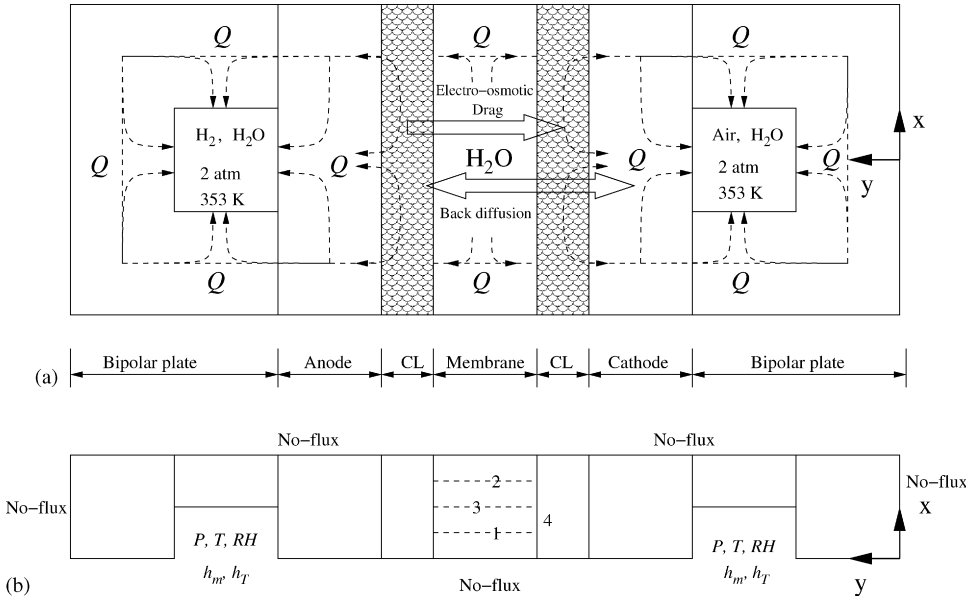

Fig. 1. (a) Schematic diagram of water transport and heat transfer in a PEM fuel cell; (b) modeling domain and boundary conditions.

ary conditions (see further below). Hence, the transient process of water transport in the backing layer is governed by diffusion only:

$$\varepsilon_g \frac{\partial c_w}{\partial t} = \nabla(D_w^g \nabla c_w) \tag{1}$$

where c_w is the water vapor concentration, ε_g is the porosity of the GDL, and D_w^g is the gaseous water diffusivity.

In the membrane, the movement of protons tends to drag water molecules with them from the anode towards the cathode, the so-called electro-osmotic drag effect. On the other hand, water is produced at the cathode catalyst layer. The electro-osmotic drag is thus confronted by back diffusion of produced water, which points from cathode to anode. The governing equation for water transport in the membrane can be stated as:

$$\varepsilon_m \frac{\partial c_{wm}}{\partial t} = \nabla(D_w^m \nabla c_{wm}) - \nabla\left(\frac{n_d}{F}\vec{J}_m\right) \tag{2}$$

where c_{wm} is the water concentration in the membrane, ε_m is the volume fraction of electrolyte in the membrane, D_w^m is the liquid water diffusivity in the membrane, n_d is the electro-osmotic drag coefficient, and J_m is the protonic current density in the electrolyte phase.

In the catalyst layer, both ionomer water and water vapor coexist and are taken to be in thermodynamic equilibrium locally. We assume water diffusion in the electrolyte and water vapor diffusion in the pores of the catalyst layer. The governing equation for the equilibrium system is written as follows:

$$\varepsilon_g \frac{\partial c_w}{\partial t} + \varepsilon_m \frac{\partial c_{wm}}{\partial t} = \nabla(D_w^g \nabla c_w) + \nabla(D_w^m \nabla c_{wm}) - \frac{1}{2F} R_i - \nabla\left(\frac{n_d}{F}\vec{J}_m\right) \tag{3}$$

where the two terms on the left hand side represent the water sorption in the voids and electrolyte, respectively. The third and fourth terms on the right hand side represent the water production and electro-osmotic drag, respectively. Water is produced at the cathode side catalyst layer only, hence the third term on the right hand side vanishes at the anode catalyst layer. The water concentration in the membrane, c_{wm}, is defined as:

$$c_{wm} = \frac{\rho_m \lambda}{\mathcal{W}} \tag{4}$$

where ρ_m is the dry membrane density, $\mathcal{W}$ is the equivalent molecular weight ($1.1\,\mathrm{kg\,mol^{-1}}$) of the dry membrane, and λ is the membrane water content, which denotes the number of water molecules per sulfonic acid group within the membrane. As mentioned previously, several correlations for the membrane water content have been developed in the literature. Among them, the formula developed by Springer et al. [3] was used most extensively. However, the experimental data presented by Springer et al. was measured at 30 °C, which has non-negligible differences from the data at 80 °C. This can be easily seen in Fig. 2. Therefore, an empirical formula for the experimental data at 80 °C is employed in this study [5]:

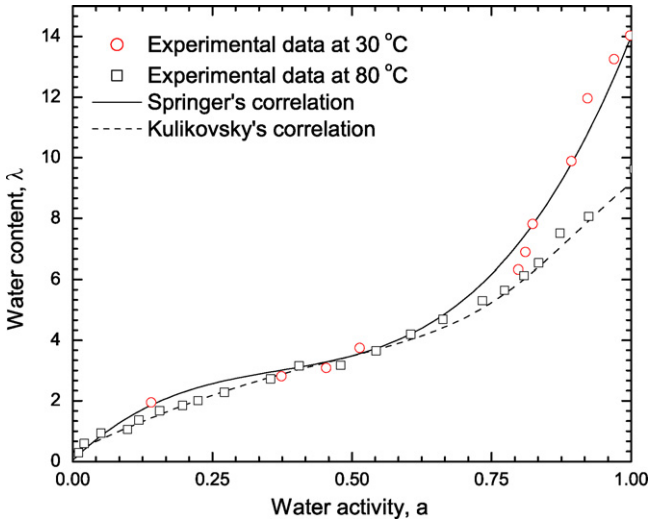

Fig. 2. Water uptake of Nafion membrane at equilibrium with water vapor.

$$\lambda = 0.3 + 6a[1 - \tanh(a - 0.5)] + 3.9\sqrt{a}\left[1 + \tanh\left(\frac{a - 0.89}{0.23}\right)\right] \tag{5}$$

In the above equation, the membrane water content is a unique function of the water activity, a, which is defined as:

$$a = \frac{c_w RT}{P^{sat}} \tag{6}$$

The water saturation pressure, P^{sat}, is determined through [3]:

$$\log_{10} P^{sat} = -2.1794 + 0.02953(T - 273) - 9.1837 \times 10^{-5}(T - 273)^2 + 1.445 \times 10^{-7}(T - 273)^3 \tag{7}$$

where P^{sat} is in units of atm and T, the temperature, is in units of Kelvin (K).

Strictly speaking, Eq. (5) is only valid for $a < 1$. However, it was extrapolated to the region $1 < a < 3$ in the present study to account for the supersaturation conditions which commonly appear in single-phase models, such as in Kulikovsky's work.

From Eqs. (4)–(6), it can be seen that the water concentration in the membrane, c_{wm}, can be converted to the water vapor concentration, c_w, through the mathematical relation [5]:

$$\frac{dc_{wm}}{dc_w} = \frac{\rho_m RT}{\mathcal{W} P^{sat}} \frac{d\lambda}{da} \tag{8}$$

Consequently, using the single-domain water transport approach [7], Eqs. (1)–(3) can be combined into a general form:

$$\varepsilon_w^{eff} \frac{\partial c_w}{\partial t} = \nabla(D_w^{eff} \nabla c_w) - \frac{1}{2F} R_i - \nabla\left(\frac{n_d}{F}\vec{J}_m\right) \tag{9}$$

where the effective porosity (ϵ_w^{eff}) and effective diffusivity (D_m^{eff}) of water transport can be evaluated according to Eq. (8) in each

layer. For example, in the catalyst layer it has the form:

$$\epsilon_{\mathrm{w}}^{\mathrm{eff}} = \epsilon_{\mathrm{g}} + \epsilon_{\mathrm{m}} \left(\frac{\mathrm{d}c_{\mathrm{wm}}}{\mathrm{d}c_{\mathrm{w}}} \right) \tag{10}$$

$$D_{\mathrm{w}}^{\mathrm{eff}} = D_{\mathrm{w}}^{\mathrm{g}} + D_{\mathrm{w}}^{\mathrm{m}} \left(\frac{\mathrm{d}c_{\mathrm{wm}}}{\mathrm{d}c_{\mathrm{w}}} \right) \tag{11}$$

Once the membrane water content is obtained from Eq. (5), the liquid water diffusivity and electro-osmotic drag coefficient can be determined with the empirical correlations given in [5]:

$$D_{\mathrm{w}}^{\mathrm{m}} = 4.1 \times 10^{-10} \left(\frac{\lambda}{25} \right)^{0.15} \left[1 + \tanh \left(\frac{\lambda - 2.5}{1.4} \right) \right] \tag{12}$$

$$n_{\mathrm{d}} = \begin{cases} 1, & \lambda < 9, \\ 0.117\lambda - 0.053, & \lambda \geq 9. \end{cases} \tag{13}$$

The membrane electrical conductivity, σ_{m} (S m^{-1}), is also a function of water content and is expressed as [3]:

$$\sigma_{\mathrm{m}} = (0.005139\lambda - 0.00326) \exp \left[1268 \left(\frac{1}{303} - \frac{1}{T} \right) \right]. \tag{14}$$

2.2. Heat transfer

Similar to the water transport, convection effects on the heat transfer are also neglected in our two-dimensional model. The general form of the energy equation can then be stated as:

$$(\rho c_{\mathrm{p}})^{\mathrm{eff}} \frac{\partial T}{\partial t} = \nabla (k^{\mathrm{eff}} \nabla T) + \dot{Q} \tag{15}$$

where $(\rho c_{\mathrm{p}})^{\mathrm{eff}}$ represents the effective heat capacity of each layer. For example, in the porous GDL we have:

$$(\rho c_{\mathrm{p}})^{\mathrm{eff}} = \epsilon (\rho c_{\mathrm{p}})_{\mathrm{g}} + (1 - \epsilon)(\rho c_{\mathrm{p}})_{\mathrm{s}} \tag{16}$$

That is, the effective value is determined by the volume fraction of each phase in the layer. The specific heat (c_{p}) of a Nafion membrane is unavailable. The specific heat of a PTFE based structure is used instead. Similarly, the effective thermal conductivity, k^{eff}, is evaluated for each layer. For example, in the catalyst layer it reads:

$$k^{\mathrm{eff}} = \epsilon_{\mathrm{w}} k_{\mathrm{w}} + \epsilon_{\mathrm{m}} k_{\mathrm{m}} + \epsilon_{\mathrm{s}} k_{\mathrm{s}} + \epsilon_{\mathrm{g}} k_{\mathrm{g}} \tag{17}$$

where ϵ_{w}, ϵ_{m}, ϵ_{s} and ϵ_{g}, represent the volume fraction of liquid water, membrane electrolyte, solid matrix and the gas pore, respectively. Hence, the summation of the ϵ terms equals 1.

The last term $\dot{Q}$ in Eq. (15) represents the heat source. The total heat generation in a PEM fuel cell is comprised of reversible and irreversible heat releases. The irreversible heat release can be further divided into activation heat generation and ohmic heating, since in the present formulation the activation polarization actually includes the overpotential due to the mass transfer. Therefore, the total heat generation is:

$$\begin{aligned} \dot{Q} &= \dot{Q}_{\mathrm{rev}} + \dot{Q}_{\mathrm{act}} + \dot{Q}_{\mathrm{ohm}} \\ &= \underbrace{\left| \frac{R_i}{nF} \right| (T\Delta S)}_{\mathrm{rev}} + \underbrace{|\eta * R_i|}_{\mathrm{act}} + \underbrace{\frac{J_{\mathrm{s}}^2}{\sigma_{\mathrm{s}}^{\mathrm{eff}}} + \frac{J_{\mathrm{m}}^2}{\sigma_{\mathrm{m}}^{\mathrm{eff}}}}_{\mathrm{ohm}} \end{aligned} \tag{18}$$

where ΔS represents the entropy change of the overall reaction, η is the activation overpotential, R_i is the reaction rate, σ_{s} and σ_{m} are the electronic and protonic conductivities, respectively, J_{s} and J_{m} are the electronic and protonic current densities, respectively. R_i, J_{s} and J_{m} will be defined in the next section.

It should be noted that the first two terms – the reversible and activation heat generation – are related to electrochemical reactions and, hence, only valid in the catalyst layers. The protonic current flows in the electrolyte. Therefore, the protonic ohmic heating source terms are considered only in the membrane and the two catalyst layers. Similarly, the electronic ohmic heating term is considered in the bipolar plates, electrodes and catalyst layers, with the membrane excluded.

2.3. Governing equations

The species and charge transport equations have been already formulated in our previous study [1]. The governing equations for the whole system can now be summarized as follows (the source terms in the subsequent equations are summarized in Table 1):

Table 1
Source terms for the conservation equations in each region

	S_{k}	S_{ϕ}	S_{T}
Bipolar plate	0	0	$\frac{J_{\mathrm{s}}^2}{\sigma_{\mathrm{s}}^{\mathrm{eff}}}$
Electrode	0	0	$\frac{J_{\mathrm{s}}^2}{\sigma_{\mathrm{s}}^{\mathrm{eff}}}$
Anode CL	$S_{H_2} = -\frac{1}{2F} R_i$ $S_{\mathrm{H_2O}} = -\nabla \left(\frac{n_{\mathrm{d}}}{F} \vec{J}_{\mathrm{m}} \right)$	R_i	$\lvert \eta * R_i \rvert + \frac{J_{\mathrm{s}}^2}{\sigma_{\mathrm{s}}^{\mathrm{eff}}} + \frac{J_{\mathrm{m}}^2}{\sigma_{\mathrm{m}}^{\mathrm{eff}}}$
Cathode CL	$S_{\mathrm{O_2}} = -\frac{1}{4F} R_i$ $S_{\mathrm{H_2O}} = -\nabla \left(\frac{n_{\mathrm{d}}}{F} \vec{J}_{\mathrm{m}} \right) - \frac{1}{2F} R_i$	R_i	$\left\lvert \frac{R_i}{4F} \right\rvert (T\Delta S) + \lvert \eta * R_i \rvert + \frac{J_{\mathrm{s}}^2}{\sigma_{\mathrm{s}}^{\mathrm{eff}}} + \frac{J_{\mathrm{m}}^2}{\sigma_{\mathrm{m}}^{\mathrm{eff}}}$
Membrane	0	0	$\frac{J_{\mathrm{m}}^2}{\sigma_{\mathrm{m}}^{\mathrm{eff}}}$

$$\text{Species}: \quad \varepsilon^{\text{eff}}\frac{\partial c_i}{\partial t} = \nabla(D_i^{\text{eff}}\nabla c_i) + S_{\text{k}} \tag{19}$$

$$\text{Electrons}: \quad 0 = \nabla(\sigma_{\text{s}}^{\text{eff}}\nabla V_{\text{s}}) - S_{\phi} \tag{20}$$

$$\text{Protons}: \quad 0 = \nabla(\sigma_{\text{m}}^{\text{eff}}\nabla V_{\text{m}}) + S_{\phi} \tag{21}$$

$$\text{Energy}: \quad (\rho c_{\text{p}})^{\text{eff}}\frac{\partial T}{\partial t} = \nabla(k^{\text{eff}}\nabla T) + S_{\text{T}} \tag{22}$$

Here, Eq. (19) describes the diffusion of O_2, N_2, and H_2O for the cathode side, and diffusion of H_2, and H_2O for the anode side. Eqs. (19)–(22) are closely coupled through the nonlinear Butler–Volmer equation:

$$R_i = aj_{0,\text{ref}}\left(\frac{c_i}{c_{i,\text{ref}}}\right)^{\gamma_i}\left\{\exp\left[\frac{\alpha_{\text{a}}nF}{\Re\text{T}}(V_{\text{s}} - V_{\text{m}})\right] - \exp\left[-\frac{\alpha_{\text{c}}nF}{\Re\text{T}}(V_{\text{s}} - V_{\text{m}})\right]\right\} \tag{23}$$

and the current densities are related to the phase potential through the following expressions:

$$\vec{J}_{\text{s}} = -\sigma_{\text{s}}^{\text{eff}}\nabla V_{\text{s}} \tag{24}$$

$$\vec{J}_{\text{m}} = -\sigma_{\text{m}}^{\text{eff}}\nabla V_{\text{m}} \tag{25}$$

2.4. Boundary and initial conditions

The boundary conditions for water transport and heat transfer processes are illustrated in Fig. 1(b). Water transport modeling usually involves the implementation of internal boundary conditions at the membrane/CL interface and/or the liquid/vapor interface. However, by using the one-equation approach in this study (Eq. (9)), the complexity of applying internal boundary conditions is simply bypassed. As a result, a convective mass transfer boundary condition is applied at the channel/GDL interface which needs the water vapor concentration to be specified in the gas channel. We use

$$\vec{n}(D_{\text{e}}^{\text{eff}}\nabla c_{\text{w}})|_{\text{electrode side}} = h_{\text{m}}(c_{\text{w},0}|_{\text{channel side}} - c_{\text{w}}|_{\text{electrode side}}) \tag{26}$$

where $\vec{n}$ denotes the unit normal vector, $c_{\text{w},0}$ is the water vapor concentration in the gas channel which is calculated based on the relative humidity, operating temperature and pressure:

$$c_{\text{w},0} = \frac{\Im P^{\text{sat}}}{RT} \tag{27}$$

Here, $\Im$ denotes the relative humidity (RH) which is one of the input parameters, P^{sat} is the saturation pressure and determined by Eq. (7). The parameter h_{m} in Eq. (26) is a mass transfer coefficient. The mass transfer of water vapor from the gas channel to the electrode surface is analogous to heat transfer in a channel with heat flux on one boundary and the other three boundaries being insulated. Therefore, h_{m} can be calculated from the Sherwood number correlation for uniform surface mass flux [17]:

$$Sh \equiv \frac{h_{\text{m}}d_{\text{h}}}{D_{\text{w}}} = 2.712 \tag{28}$$

where d_{h} represents the hydraulic diameter of the gas channel, treating the gas flow in the channel as laminar. For the other boundaries in the water transport region, *no-flux* conditions apply

$$\frac{\partial c_{\text{w}}}{\partial \vec{n}} = 0 \tag{29}$$

In the heat transfer domain, convective heat transfer boundary conditions are applied on all gas channel boundaries:

$$\vec{n}(k^{\text{eff}}\nabla T)|_{\text{solid side}} = h_{\text{T}}(T_0|_{\text{channel side}} - T|_{\text{solid side}}) \tag{30}$$

where the temperature at the gas channel T_0 is kept constant at 353 K; h_{T} is the convective heat transfer coefficient, which can be derived from the Nusselt number correlation [17]

$$Nu \equiv \frac{h_{\text{T}}d_{\text{h}}}{k_i} = 3.61 \tag{31}$$

Here, k_i denotes the thermal conductivity of the gas mixture, i.e. humidified hydrogen at the anode gas channel and humidified air at the cathode gas channel.

For the other boundaries in the heat transfer region, *periodic* (or *thermal insulation*) boundary conditions apply. To leading order and for the purpose of this study, this is the case for fuel cell stacks. The initial conditions are simply the steady state fields of the previous operating point.

2.5. Numerical procedures

The conservation equations are solved using *COMSOL Multiphysics*™, a commercial software package based on finite element methods. The GMRES linear system solver with the *Geometric Multigrid* preconditioner is selected to accelerate the computation. Variant time stepping is used in which a small constant time step is used at the first few time steps to capture the relatively fast species transport phenomena, and a larger time step is chosen for the rest of the time period for the slower water transport and heat transfer processes. To accurately describe the electrochemical phenomena, the element size in the catalyst layer is refined to no more than 1/10 of the catalyst layer thickness and the resulting mesh has approximately 4×10^5 degrees of freedom (DOF). It takes about 1 h to run a transient case on a 64-bit Linux machine with dual core processor at 2.8 GHz and 4 GB memory.

3. Results and discussion

In our base case, the gas feeds are assumed to be fully humidified (100% relative humidity) at a temperature of 353 K and a pressure of 2 atm. Water condensation and the ensuing two-phase phenomena exceed the scope of the present study but will be incorporated in our future studies. Thus, the relative humidity may exceed 1 in some regions where the water vapor can be assumed to be in a supersaturated state. The thermal and physical properties used in the model are listed in Table 2; other parameters such as the geometric dimensions and kinetic parameters can be found in [1]. For comparison purposes, three kinds of membranes (Nafion 112, Nafion 115, Nafion 117) are

Table 2
Thermal and physical properties of some materials @ 353 K [18,22]

	Density (kg m^{-3})	Thermal conductivity (W m^{-1} K)	Specific heat (J kg^{-1} K)
Bipolar plate	1900	21	710
Electrode support (PTFE)	2200	1.3 (Ballard AvCarb® P150)	1050
Catalyst layer	2100	0.8725	1050
Membrane (Nafion)	1980	0.445	1050 (PTFE)
Hydrogen	0.069	0.204	14400
Air	0.9950	0.03	1010
Water vapor	0.632	0.023	1960
Liquid water	972	0.67	4197

modeled in this work. Studies [19] have revealed that Nafion 115 and Nafion 117 membranes have very similar microstructures, but the Nafion 112 microstructure differs from that of Nafion 115 and Nafion 117 in the crystalline component of the PTFE backbone. Consequently, Nafion 112 possesses different membrane properties from Nafion 115 and Nafion 117, such as the permeability, water uptake values, etc. In this study, however, we assume all Nafion membranes have the same physical properties. They differ from each other only by the thickness. The thickness of a dry membrane Nafion 112, Nafion 115, and Nafion 117 is 50.8 μm, 127 μm, and 177.8 μm, respectively. They increase linearly with an increase in membrane water content λ [3]. Therefore, the membrane thickness in PEMFCs under the working conditions is usually adjusted by using certain expansion coefficients to account for the swelling effect during the membrane water uptake. In this study, some typical thickness values which are widely employed in the literature (50 μm for Nafion 112 [20], 164 μm for Nafion 115 [21], and 230 μm for Nafion 117 [12]) are used to qualitatively demonstrate the effect of membrane thickness on the cell dynamic performance.

Proton transport in the membrane will cause membrane potential losses due to ohmic effects. It is usually called membrane ohmic overpotential. Physically, the ohmic potential loss is proportional to the resistor length and inversely proportional to the electrical conductivity. Provided that the conductivity of Nafion 112, Nafion 115, and Nafion 117 are the same, it can be inferred that the membrane ohmic overpotential will be determined by the membrane thickness, and hence the overpotential increases are in the order of Nafion 112, Nafion 115, and Nafion 117. In other words, the cell performance decreases in the same order. This conclusion is verified by the polarization curves shown in Fig. 3. Moreover, for the same kind of membrane, such as Nafion 117, the ohmic overpotential is determined by the electrical conductivity which, in turn, is determined by the membrane water content. The membrane water content, and thus the electrical conductivity, is higher under isothermal conditions where we find generally lower temperature than for the non-isothermal case. Therefore, the isothermal case shows better performance than the non-isothermal one, as shown in Fig. 3. This trend also applies to Nafion 112 and Nafion 115, although they are not shown in the figure.

To better understand the transient processes within a working PEM fuel cell, separate water transport and heat transfer studies are conducted using Nafion 117. Fig. 4 exhibits the dynamic responses of current density with respect to a step voltage change from 0.5 to 0.6 V. In Fig. 4(a), the water transport sub-model is switched off and the membrane electrical conductivity is assumed to be constant at 0.10 S cm^{-1} [22]. The figure shows that an abrupt undershoot exists at the initial stage which is caused by the species transient transport, then the cell gradually reaches steady state at around 12 s. Recall that the time scale of species transfer is about 1 s, as shown in our previous study [1]. Therefore, the prolonged time periods must be brought by the heat transfer process. In Fig. 4(b), the water transport sub-model is switched on, whereas the cell is assumed isothermal at 353 K. It can be seen that due to the sluggishness of water transport, the cell current density varies more smoothly compared to the first case, and the state steady is reached at around 40 s. If the water transport and heat transfer sub-model are applied simultaneously, as shown in Fig. 4(c), it is seen that the cell current density experiences an overshoot right after the undershoot and the steady state is further extended to around 80 s. The undershoot is still caused by the species transport where the species concentration remains low as in the higher current density state. As for the overshoot, there are two reasons. Firstly, the temperature varies relatively slowly as the working conditions are being changed. Therefore, the temperature remains high at the initial stage as in the higher current density state. Higher temperature results in better performance of the electrochemical reactions, thus an overshoot follows. A more important reason for the current overshoot is that the decrease of temperature induces the

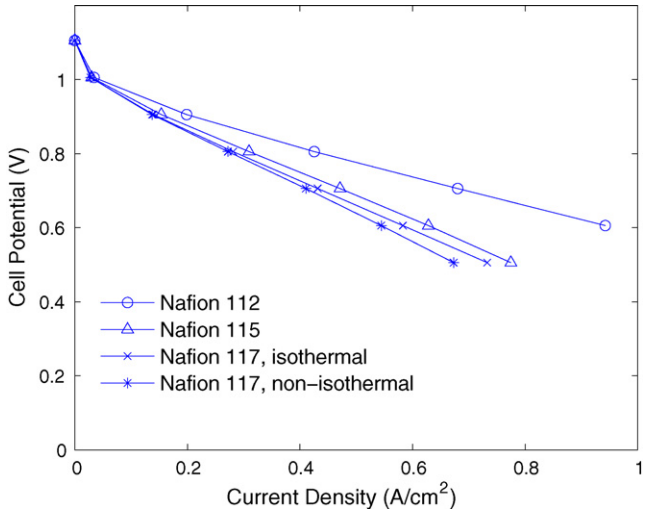

Fig. 3. Polarization curves at steady state.

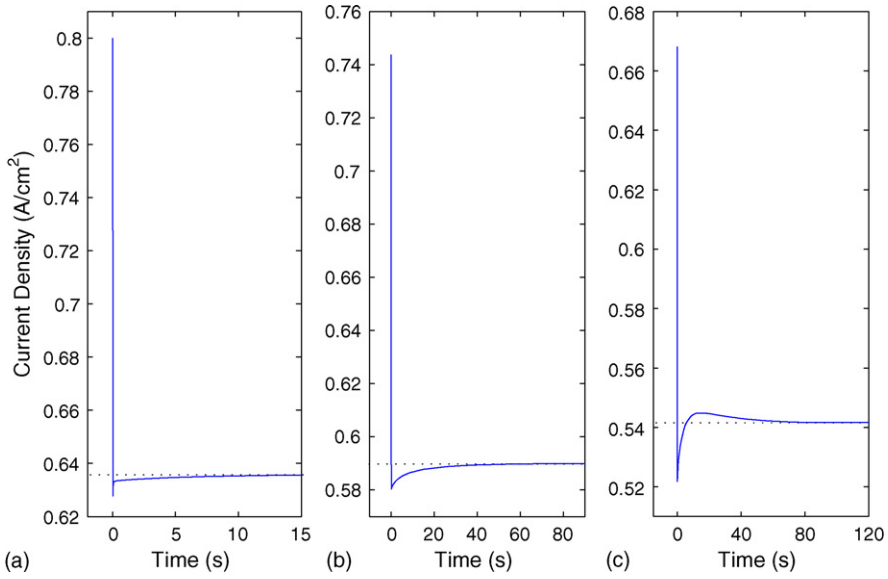

Fig. 4. Transient variation of current density with respect to a step voltage change (0.5–0.6 V) using membrane Nafion 117: (a) water transport sub-model switched off; (b) heat transfer sub-model switched off; (c) both water transport and heat transfer sub-model switched on.

decrease of saturation pressure as well (refer to Eq. (7)), which in turn results in the increase of water activity and membrane water content (refer to Eqs. (6) and (5)). The results indicate that the membrane water content is slightly increased when the cell voltage is switched from 0.5 V to 0.6 V, although there is more water being produced at 0.5 V. This again demonstrates the significance of the inclusion of thermal effects.

Fig. 5 compares the dynamic responses of the cell corresponding to a step voltage decrease from 0.7 to 0.6 V, by using three different membrane schemes. For Nafion 117 (Fig. 5(c)), the trend of variation is much like the reverse of Fig. 4(c). They do have slight differences though. It is observed that the voltage decrease case (Fig. 5(c)) reaches steady state at about 70 s, slightly faster than the voltage increase case (Fig. 4(c)). The dynamic response of the cell using Nafion 115 is similar to that of Nafion 117, but the response time is reduced to around 40 s due to the reduced membrane thickness, as shown in Fig. 5(b). For Nafion 112, water can be readily removed or supplied in the thin membrane and Fig. 5(a) shows that there is no obvious undershoot before the cell reaches steady state at about 15 s.

The membrane water content at two membrane cross sections (line 1 & 2, shown in Fig. 1(b)) is shown in Fig. 6. Line 1 and 2 represent the region of the membrane under the flow channel and the channel land, respectively. At constant cell voltage of 0.6 V, it is seen that the water content of Nafion 117 is higher than Nafion 112 in both locations. This is due to the temperature and electro-osmotic drag effect. From the polarization curves in Fig. 3, it follows that the current density for Nafion 112 and Nafion 117

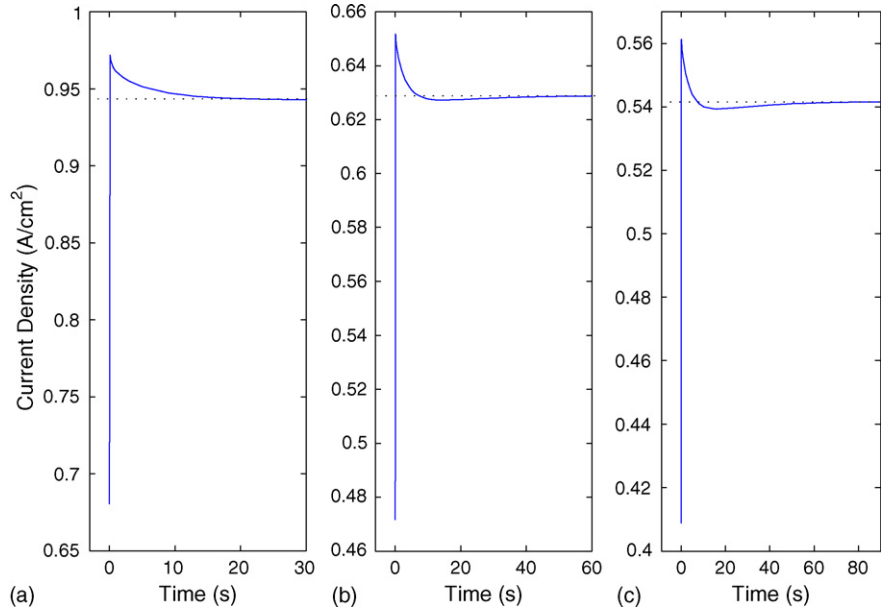

Fig. 5. Transient variation of current density with respect to a step voltage change (0.7–0.6 V) using membrane: (a) Nafion 112; (b) Nafion 115; (c) Nafion 117.

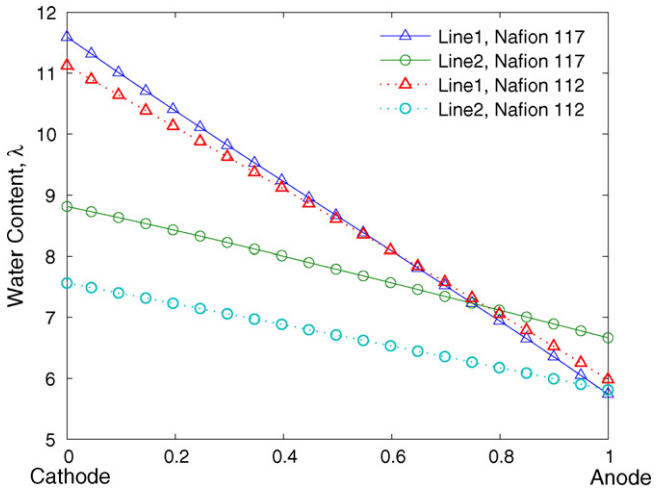

Fig. 6. Membrane water content on line 1 and line 2 (shown in Fig. 1(b)) at the cell voltage of 0.6 V.

at 0.6 V are about 0.95 and 0.54 A cm^{-2}, respectively. Therefore, the temperature and electro-osmotic drag in the Nafion 112 membrane is higher than in Nafion 117. The water content and electrical conductivity in Nafion 112 are hence lower than in Nafion 117. Furthermore, it is apparent that the water content always decreases from the cathode side towards the anode. In Nafion 117, the two curves intersect at around 0.75 of the non-dimensionlized membrane thickness, which suggests that at this location the membrane water content under the channel area is the same as under the land. Past this point, the water content under the channel becomes higher. In contrast, in a Nafion 112 membrane the water content under the land is always higher than that under the channel.

Fig. 7 demonstrates the transient variation of the water content along the center cross section of Nafion 117 (line 3) and along the membrane/catalyst layer interface (line 4) (shown in Fig. 1(b)) with respect to a relative humidity decrease from 1 to 0.5. Fig. 7(a) shows that the membrane water content varies

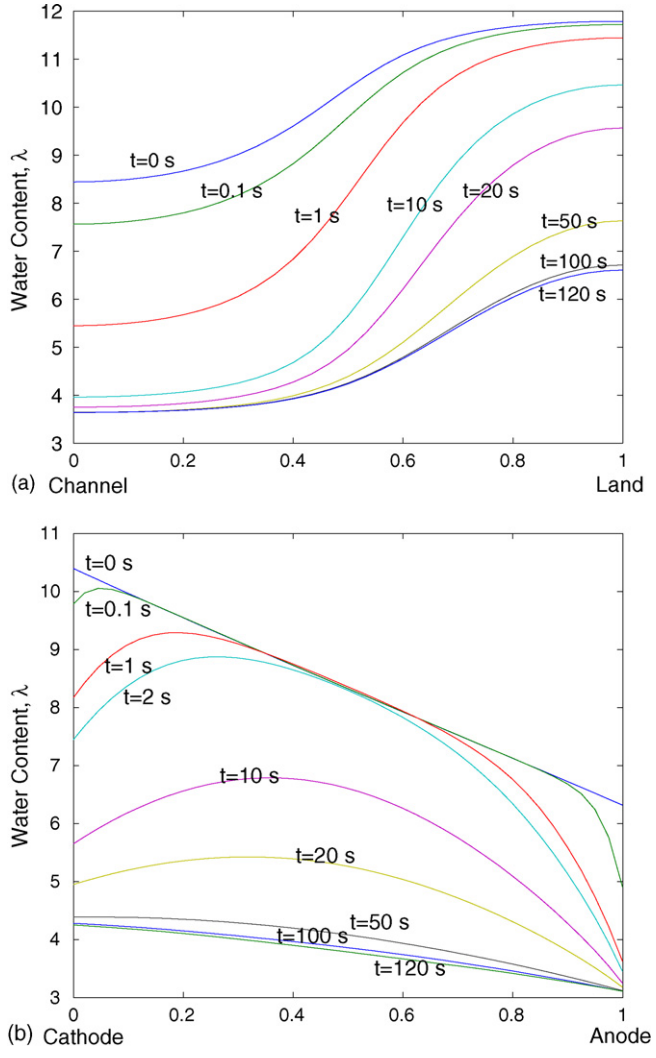

Fig. 7. Transient variation of the membrane water content corresponding to a relative humidity decrease from 1 to 0.5 (Nafion 117, cell voltage 0.6 V): (a) on line 4; (b) on line 3 (refer to Fig. 1(b)).

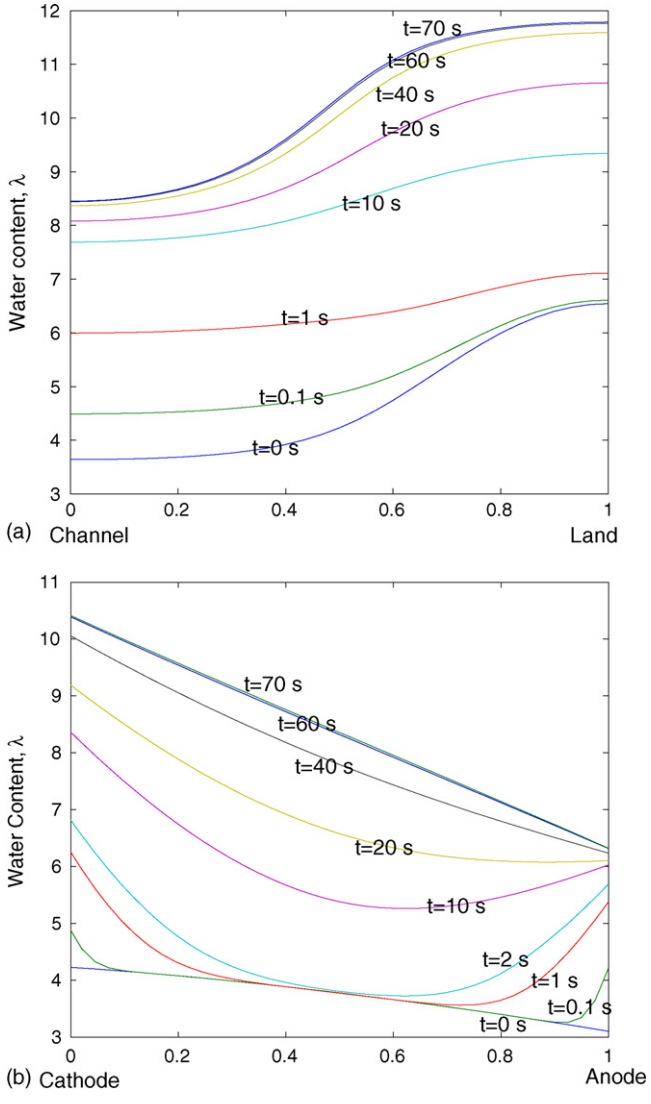

Fig. 8. Transient variation of the membrane water content corresponding to a relative humidity increase from 0.5 to 1 (Nafion 117, cell voltage 0.6 V): (a) on line 4; (b) on line 3 (refer to Fig. 1(b)).

faster under the channel than under the land, because the water vapor under the channel area is more readily removed. The variation diminishes at around 50 s under the channel, but diminishes at around 120 s under the land area. In the membrane transverse direction (line 3), Fig. 7(b) exhibits that the water content first decreases at the two interfaces (anode and cathode), then the variation evolves gradually towards the center. At around 2 s, the water content in the whole region begins to drop. The water content distribution follows a parabolic-like curve during the variation. The evolution subsides at around 120 s, similar to the dynamics shown on line 4.

Fig. 8 presents the transient variation of the water content on line 3 and line 4 (refer to Fig. 1(b)) of Nafion 117 with respect to a relative humidity increase from 0.5 to 1. On line 4 (Fig. 8(a)), the water content under the flow channel adjusts to the relative humidity increase very quickly due to the fast water vapor diffusion from the gas channel. At around 1 s, the water content is almost uniform. Between 1 and 10 s, the water content in the whole membrane increases rather uniformly. At around 40 s, the membrane region under the channel reaches steady state first; the water content under the land region keeps on increasing and reaches steady state at about 60 s. Fig. 8(b) represents the transient variation of the water content on line 3. Very similar to Fig. 7(b), the variation starts from the two ends, then evolves towards the middle. At around 2 s, the water content in the whole region begins to increase in a parabolic manner. The evolution slows down at 60 s and the cell reaches equilibrium. Comparing Fig. 8 with Fig. 7, we can also find that the cell responses faster when the relative humidity increases rather than decreases, last but not least because of nonlinear water diffusion in the membrane.

The temperature variation in Nafion 117, corresponding to a relative humidity decrease (1–0.5), is presented in Fig. 9. Generally speaking, the variations of temperature along both directions (line 3 and line 4) are more uniform compared with the variation of the water content, and the transient variation curves are almost parallel to each other. The thermal conductivity of hydrogen is several times higher than that of air (refer to Table 2). Therefore, more heat is removed from the anode gas channel and the temperature decreases from the cathode to the anode, as shown in Fig. 9(b). Also, the reversible cathodic reaction is exothermic while the reversible anodic reaction is endothermic, i.e. more heat is released in the cathodic reaction than in the anodic reaction. The steady state of temperature distribution is achieved around 120 s, the same as for the water content.

Fig. 10 compares the dynamic responses of three different membranes for the relative humidity changes. It can be seen that the response time increases from Nafion 112 to Nafion 117, due to the increased membrane thickness. Moreover, it is seen that the cell experiences longer response time when the relative humidity decreases rather than increases. Using Nafion 117 as an example, the response time is about 120 s as the relative humidity is decreased from 1 to 0.5. However, the response time is only about 60 s as the relative humidity is increased from 0.5 to 1.

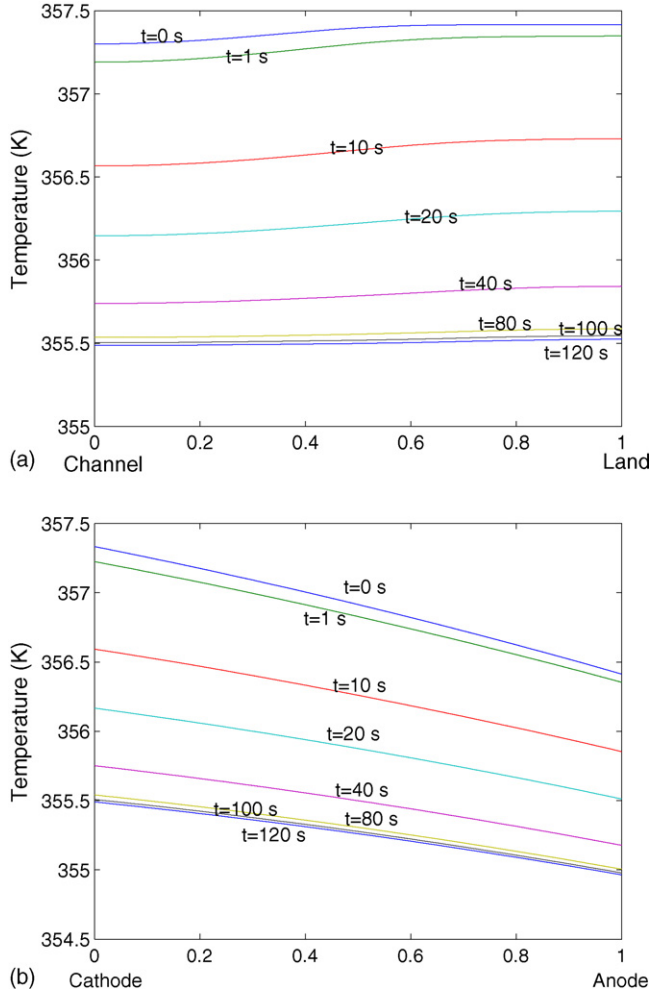

Fig. 9. Transient variation of the temperature corresponding to a relative humidity decrease from 1 to 0.5 (Nafion 117, cell voltage 0.6 V): (a) on line 4; (b) on line 3 (refer to Fig. 1(b)).

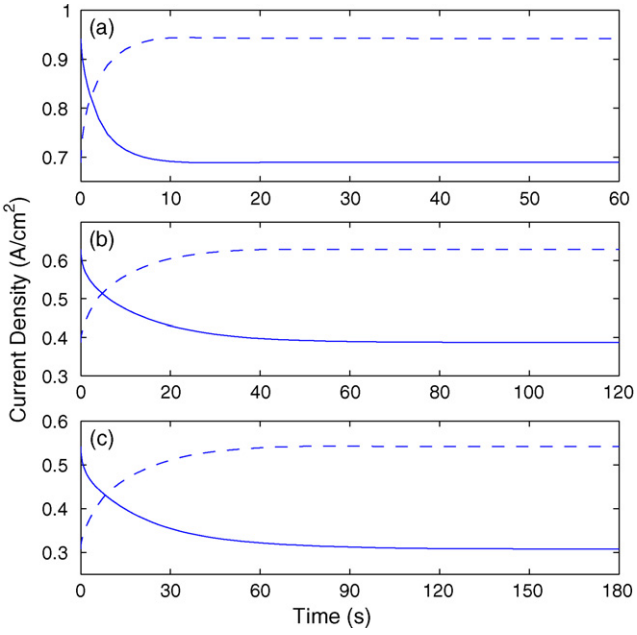

Fig. 10. Transient variation of the current density with respect to the relative humidity changes (solid line: 1–0.5; dashed line: 0.5–1): (a) Nafion 112; (b) Nafion 115; (c) Nafion 117.

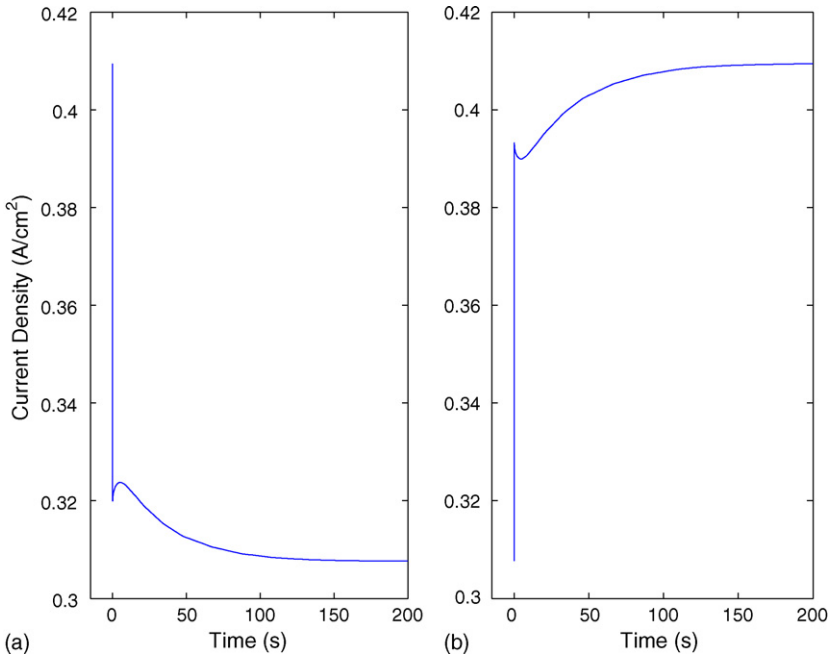

Fig. 11. Dynamic response of the current density at the relative humidity of 0.5 using membrane Nafion 117: (a) voltage change from 0.5 to 0.6 V; (b) voltage change from 0.6 to 0.5 V.

The cell dynamic performance under low relative humidity working conditions is also studied and the results for Nafion 117 are demonstrated in Fig. 11. It clearly shows that the cell dynamic characteristics at lower relative humidity are totally different from that at fully humidified operation (Figs. 4(c) and 5(c)). This is mainly because the membrane can take up more water under lower relative humidity conditions than at fully humidified conditions. In Fig. 11(a), the cell voltage is switched from 0.5 to 0.6 V. An undershoot occurs at the initial stage due to the low species concentrations. With the recovery of reactant species supply and due to the relatively higher temperature and hence better electrochemical performance at the initial stage, the cell current density increases and an overshoot appears. On the other hand, a large amount of water is accumulated in the membrane at the initial higher current density state. Therefore, the membrane dehydrates gradually due to the reduced water production at lower current density. Accordingly, the cell current density decreases gradually till it reaches an equilibrium state at around 160 s. In Fig. 11(b), a reverse transient curve exhibits a cell voltage decrease from 0.6 to 0.5 V. An undershoot follows an overshoot due to the species transient, then the current density gradually increases during the membrane hydration process and reaches steady state around 140 s. Comparing Fig. 11 with Figs. 4(c) and 5(c), it surprisingly reveals that the response times are almost doubled when the relative humidity is reduced by a half.

4. Conclusions

A comprehensive transient model which accounts for all four transient processes, namely, species transport, electric double layer charge/discharge, membrane water uptake, and heat transfer, is implemented in this study. By using different membrane types, i.e. Nafion 112, Nafion 115, and Nafion 117, the effect of the membrane thickness on the dynamic cell performance is studied. The results show that the cell dynamic response time increases with the membrane thickness and the Nafion 112 membrane presents the best dynamic performance.

The membrane hydration/dehydration processes are analyzed through the transient water content distribution along two different directions. The results reveal that the membrane becomes hydrated/dehydrated faster in the region under the channel than under the land. The inclusion of heat transfer processes has significant influence on the dynamic cell response. The current density varies monotonically if the cell is isothermal. In contrast, both current overshoot and undershoot occur if the temperature effect is accounted for.

Numerical studies on the change of cell working conditions show that the dynamic cell response is not symmetric under symmetric changes in working conditions. The cell response is slower if the cell voltage is increased or the relative humidity is decreased, both resulting in a current density decrease. On the other hand, when the cell operates at low relative humidity conditions, the dryer membrane can uptake and reserve more water than the fully humidified membrane. Thus, the dynamic response of the cell becomes more sluggish. The response time can be doubled if the relative humidity is reduced by half.

In summary, heat transfer effects have a substantial impact on transient modeling results. This might be amplified in our future two-phase modeling efforts.

Acknowledgements

The financial support by the Natural Sciences and Engineering Research Council (NSERC) of Canada as well as MITACS (NCE) is greatly appreciated.

References

[1] H. Wu, X. Li, P. Berg, Int. J. Hydrogen Energy, in press.
[2] G.J.M. Janssen, M.L.J. Overvelde, J. Power Sources 101 (2001) 117–125.
[3] T.E. Springer, T.A. Zawodzinski, S. Gottesfeld, J. Electrochem. Soc. 138 (1991) 2334–2342.
[4] C.R. Yang, Performance of nafion/zirconium phosphate composite membranes in PEM fuel cells, PhD Thesis, Department of Mechanical Engineering, Princeton NJ, Princeton University, 2003.
[5] A.A. Kulikovsky, J. Electrochem. Soc. 150 (11) (2003) A1432–A1439.
[6] J.T. Hinatsu, M. Mizuhata, H. Takenaka, J. Electrochem. Soc. 141 (6) (1994) 1493–1498.
[7] S. Um, C.Y. Wang, J. Power Sources 156 (2006) 211–223.
[8] P. Berg, K. Promislow, J.S. Pierre, J. Stumper, B. Wetton, J. Electrochem. Soc. 151 (3) (2004) A341–A353.
[9] J.J. Baschuk, X. Li, J. Power Sources 142 (2004) 134–153.
[10] H. Ju, H. Meng, C.Y. Wang, Int. J. Heat Mass Transfer 48 (2005) 1303–1315.
[11] A. Rowe, X. Li, J. Power Sources 102 (2001) 82–96.
[12] T. Berning, D.M. Lu, N. Djilali, J. Power Sources 106 (2002) 284–294.
[13] P. Berg, K. Promislow, J. Stumper, B. Wetton, J. Fuel Cell Sci. Tech. 2 (2005) 111–120.
[14] J. Stumper, H. Haas, A. Granados, J. Electrochem. Soc. 152 (4) (2005) A837–A844.
[15] D. Natarajan, T.V. Nguyen, J. Electrochem. Soc. 148 (12) (2001) A1324–A1335.
[16] Y. Wang, C.Y. Wang, Electrochimica Acta 50 (2005) 1307–1315.
[17] R.K. Shah, A.L. London, Laminar Flow Forced Convection in Ducts, Academic Press, NY, 1978.
[18] F.P. Incropera, D.P. Dewitt, Fundamentals of Heat and Mass Transfer, fifth ed., John Wiley & Sons, 2002.
[19] S. Sportsman, D. Way, G. Pez, The 13th annual meeting of the North American Membrane Society, Long Beach, California, 2002.
[20] G.Y. Lin, W.S. He, T.V. Nguyen, J. Electrochem. Soc. 151 (12) (2004) A1999–A2006.
[21] J.J. Baschuk, X. Li, J. Power Sources 86 (2000) 181–196.
[22] E.I. du Pont de Nemours and Company, http://www.dupont.com.